Multi-Controllability of Ambipolar Photoconductivity in Transition Metal Dichalcogenides van der Waals Heterostructures

Ahmed Elbanna, Zeng Wang, Yuanda Liu, Qing Yang Steve Wu, Xinan Liang, Hongfei Liu, Zi-En Ooi, Mengting Jiang, Jie Deng, Handong Sun, Jisheng Pan, Ze Xiang Shen, and Jinghua Teng**

A. Elbanna, Z. Wang, Y. Liu, Q. Wu, X. Liang, H. Liu, Z. Ooi, M. Jiang, J. Deng, J. Pan, J. Teng

Institute of Materials Research and Engineering (IMRE), Agency for Science, Technology and Research (A*STAR), 2 Fusionopolis Way, Singapore 138634, Singapore.

E-mail: jh-teng@imre.a-star.edu.sg

A. Elbanna, H. Sun, Z. Shen

Division of Physics and Applied Physics, School of Physical and Mathematical Sciences, Nanyang Technological University, 50 Nanyang Avenue, Singapore 637371, Singapore.

The Photonics Institute and Center for Disruptive Photonic Technologies, Nanyang Technological University, 50 Nanyang Avenue, Singapore, 639798 Singapore.

E-mail: zexiang@ntu.edu.sg

Abstract:

Two-dimensional transition metal dichalcogenides (TMDs) and their van der Waals heterostructures possess great potential for optoelectronic applications thanks to their strong quantum confinement and flexibility in bandgap engineering. Photodetection based on TMDs utilizing photoconductance typically exhibit positive photoconductance resulting from the generation of photocarriers upon illumination. Here, we report a $SnSe_2/MoS_2$ photodetector operating over a broadband range from deep ultraviolet to infrared wavelengths with not only a high responsivity and self-powered feature but also ambipolar photoresponse with both positive and negative photoconductances to multi-control parameters of wavelength, gate voltage and laser power. The transition from positive to negative photoconductance by gate voltage and laser power indicates that charge recombination and interlayer exciton trapping result in negative photoconductance. The coexistence and controllable positive and negative photoconductance hold potentials for multifunctional optoelectronic devices responding to multi-control parameters.

Keywords:

2D materials, transition metal dichalcogenides, van der Waals heterostructures, photodetectors, ambipolar photoresponse, negative photoconductance.

1. Introduction

Photodetectors (PDs) are crucial components for many applications including imaging, optical communication, chemical analysis, environmental monitoring, security and defence[1]. The emergence of two-dimensional (2D) materials opens a new avenue for high-performance PDs due to their strong light-matter interactions and thickness-tunable bandgaps[2,3]. 2D transition metal dichalcogenides (TMDs) receive particular attention for their high optical absorption (up to 10% of the sunlight for monolayer) and flexibility in bandgap engineering through controlling the band alignment in TMD heterostructures[4–6]. Type-II band alignment in TMD van der Waals heterostructures facilitates the charge extraction for faster and higher photoresponse, and allows broadband and multifunctional photodetection leveraging their interlayer excitons[7,8]. Higher photocurrents and enhanced responsivities are achieved by optimizing the charge transfer process in TMD heterostructures with large band offsets,[9] while self-powered PDs are demonstrated by choosing the constituent materials to form p-n junctions[10–14].

PDs from 2D materials and their heterostructures normally exhibit a positive photoconductance (PPC),[3,13,15] referring to the increase in the electrical conductivity of the semiconductor upon illumination with light of energy higher than the bandgap due to the creation of excess mobile charges (electrons or holes). Conversely, when the electrical conductivity of the semiconductor decreases upon light illumination, it is known as negative photoconductance (NPC). While NPC and its associated ambipolar features are promising for various applications, such as weak light detection, gas sensing, non-volatile memory, and high-speed optoelectronic devices[16–18], there are only few reports about ambipolar photoresponse in 2D materials-based PDs with limited operation bandwidth and lack of versatile control [19–24].

Here we report a 2D PD made of n^+-$SnSe_2$/n-MoS_2 heterojunction with a large band offset in the type-II band alignment. The PD showed high responsivity and broadband operation in the wavelength range of 266 nm-1100 nm, and ambipolar photoresponse with PPC in the ultraviolet (UV) – visible (VIS) range (λ=266-700 nm) and NPC in the near infrared (NIR) range (λ=800-1100 nm). The crossover wavelength from PPC to NPC can be effectively controlled via gate voltage and incident laser power. Furthermore, the PD exhibits a photoresponsivity of 3.50×10^3 AW^{-1} at 266 nm, surpassing most reported UV PDs reported in the literature[25]. Moreover, it operates efficiently in self-powered mode in the UV-VIS range due to the formation of unilateral depletion region at the n^+n junction. This 2D heterostructure PD provides a solid platform for ambipolar phenomena study and multifunctional optoelectronic device development.

2. Results and Discussion

2.1. Opto-electronic characteristics

Figure 1a shows a schematic of the type-II band alignment for $SnSe_2$ and MoS_2 monolayers based on their conduction band minimum (CBM) and valence band maximum (VBM) relative to vacuum[26]. $SnSe_2$ in bulk and monolayer form is indirect bandgap semiconductor, with energy gaps of 1.07 and 1.69 eV, respectively[27]. Few-layer (nL) $SnSe_2$ was chosen in this work for its high carrier density and mobility[28]. Meanwhile, monolayer (1L) MoS_2 was used for all the device fabrication and transferred onto the top of $SnSe_2$ to form nL $SnSe_2$/1L MoS_2 heterostructure. Under this configuration, the absorption at the heterojunction can be maximized, and the band offset between the CBM of MoS_2 and $SnSe_2$ can be maximized, thereby promoting the extraction of photogenerated carriers.

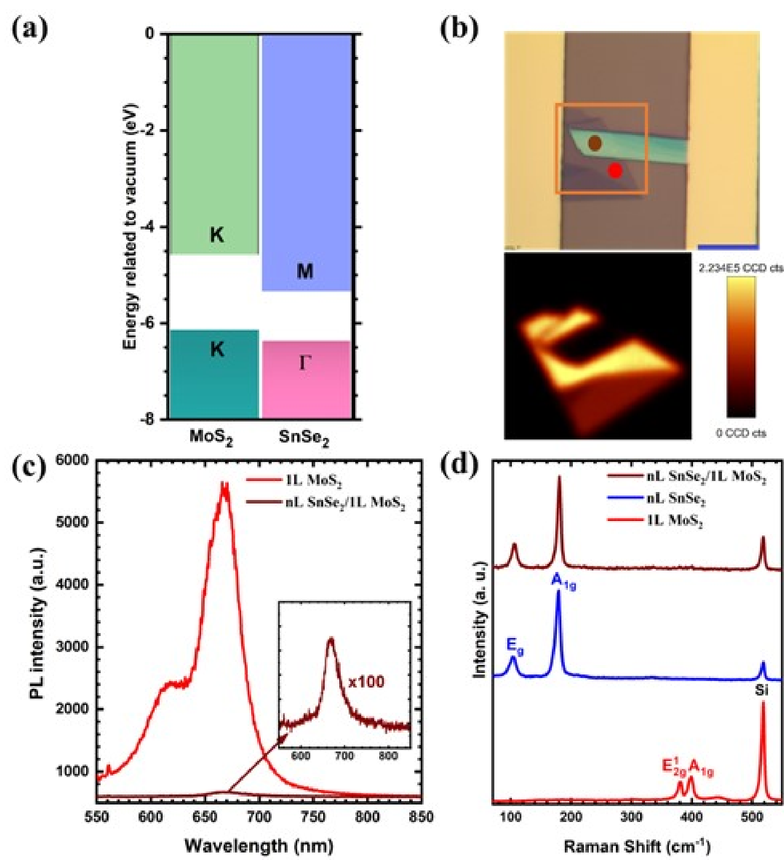

Figure 1. (a) Energy band diagram illustrating the type II band structure of MoS_2 and $SnSe_2$ atomic layers. (b) Optical microscope image of a typical nL $SnSe_2$/1L MoS_2 device and the corresponding photoluminescence (PL) mapping (orange square). The scale bar is 10 µm. (c) PL Spectra of 1L MoS_2 and $SnSe_2/MoS_2$ heterostructure measured at the position of the red and brown dot in b, respectively. The inset is the zoom-in PL spectrum for the heterojunction. (d) Raman spectra for the individual materials and heterojunction.

The microphotograph of a typical $SnSe_2/MoS_2$ device is shown in the top panel of Figure 1b with $SnSe_2$ thickness measuring approximately 43 nm by atomic force microscopy (AFM) (Figure S1, Supporting Information (SI)). The bottom panel of Figure 1b displays the photoluminescence (PL) mapping (the orange square area) under 532 nm laser excitation. The strong PL quenching at the heterojunction region, as shown in the PL spectra in Figure 1c for the overlapping area compared to 1L MoS_2 (brown and red dot position in Figure 1b, respectively), indicates the ultrafast charge transfer process across the interface between $SnSe_2$ and MoS_2. The peaks at ~670

nm and ~620 nm for 1L MoS_2 are correlated to A and B excitons, respectively[29]. It has been reported that decreasing the thickness of $SnSe_2$ resulted in a PL enhancement of $SnSe_2/MoS_2$ by a nonradiative energy transfer process[30]. In our heterostructure, the relatively thick $SnSe_2$ results in strong PL quenching. Raman spectra of individual materials and heterojunction are shown in Figure 1d. The two peaks for 1L MoS_2 observed at 381.1 cm^{-1} and 399.4 cm^{-1} can be assigned to the in-plane E^1_{2g} and the out-of-plane A_{1g} modes of MoS_2[29,31]. The specific frequency difference is 18.3 cm^{-1}, confirming that the MoS_2 is a monolayer[32]. For $SnSe_2$, the E_g and A_{1g} modes are observed at 105.3 cm^{-1} and 180.8 cm^{-1}, respectively[28,30]. Notably, the Raman peaks of MoS_2 exhibit a strong suppression at the heterojunction, which is attributed to the ultrafast interlayer charge transfer process compared to the slower carrier scattering with optical phonons[30].

The electrical properties of $SnSe_2$, MoS_2, and $SnSe_2/MoS_2$ devices were investigated under vacuum (~10^{-2}-10^{-3} mbar) using a Janis probe station (Figure S2, SI). From the transfer characteristics curves, the carrier mobilities are calculated from the maximum transconductance using the following equation:

$$\mu = \frac{(dI_{ds}/dV_g)\ L}{W\ V_{ds}\ C_i} \tag{1}$$

where L and W are the length and width of the channel, and C_i is the capacitance of 285 nm SiO_2/Si (11 $nFcm^{-2}$) used as the substrate for the device fabrication. The calculated mobilities for 1L MoS_2, nL $SnSe_2$, and nL $SnSe_2$/1L MoS_2 devices were 12.2, 36.5, and 36.2 $cm^2V^{-1}s^{-1}$, respectively. It is worth noting that the $SnSe_2$ transistor cannot be turned off within the measured range from -60 to 60 V, which is attributed to the thick $SnSe_2$ in our device. Previous investigations conducted on $SnSe_2$ field-effect transistors have also observed similar characteristics, indicating that the limiting factor is the flake thickness compared to the maximum depletion width[28,33,34]. With a fully depleted

device, the transistor can be turned off with an on-off ratio of ~10^5 at 78 K[28]. The enhanced mobility of the $SnSe_2/MoS_2$ heterojunction device as compared to MoS_2 is a result of the higher mobility of $SnSe_2$ than MoS_2.

The broadband photoresponse of the $SnSe_2/MoS_2$ heterojunction PD was measured under laser illumination at **λ**= 266-1100 nm, as described in detail in the Experimental Section. From the photocurrent, the responsivity (R) is calculated using the following equation:

$$R = \frac{I_{ph}}{P_{device}} \tag{2}$$

where,

$$I_{ph} = I_{light} - I_{dark} \tag{3}$$

And

$$P_{device} = \frac{P_{in} A_{device}}{A_{laser}} \tag{4}$$

The I_{ph} and P_{device} are the photocurrent and the effective laser power on the device area. I_{light} and I_{dark} are the measured currents with and without illumination, respectively. P_{in}, A_{device}, and A_{laser} are the incident laser power, the effective sample area, and the laser spot area, respectively. The external quantum efficiency (EQE) is calculated as:

$$EQE = \frac{h\, c\, R}{e\, \lambda} \tag{5}$$

where h, c, and e denote Planck's constant, the speed of light, and unit charge, respectively.

Assuming the shot noise dominated the total noise of the PD, the detectivity can be calculated using the following equation:[35–38]

$$D^* \approx \frac{R\sqrt{A_{device}}}{\sqrt{2eI_{dark}}} \quad (6)$$

To characterize the temporal photoresponse of the PD, we fit the rise and fall times under modulated illumination to an exponential function, defining the time required for the signal to rise from 10% to 90% and fall from 90% to 10%.

2.2. UV photoresponse

Figure 2a shows a schematic of the $SnSe_2/MoS_2$ heterojunction PD and a typical microphotograph of the fabricated device with the $SnSe_2$ of ~30 nm thick. The thickness measurements and more microphotographs of fabricated devices can be found in Figure S1, SI. The I_{ds}-V_{ds} curve (Figure 2b) exhibits a typical diode behavior with a large rectification ratio of 10^3. At the heterostructure, n^+n junction is formed due to the high intrinsic electron density of $SnSe_2$[28,34] compared to MoS_2[39]. The deep UV photoresponse of the heterojunction PD at λ= 266 nm under different illumination powers is shown in Figure 2c. From the I_{ds}-V_{ds} curves, the responsivity and EQE values of the heterojunction PD are calculated and shown in Figure 2d as a function of the illumination power.

Notably, a high responsivity of 3.5×10^3 AW^{-1} and EQE of 1.6×10^6 % are achieved at 1 μW laser illumination. Figure S3, SI shows the UV photoresponse of individual $SnSe_2$ and MoS_2 materials. Comparatively, the $SnSe_2/MoS_2$ heterojunction PD exhibits a responsivity value three and two orders of magnitude higher than that of MoS_2 and $SnSe_2$ based PDs, respectively. The type-II band alignment at the heterostructure with a large CBM offset and the formation of unilateral depletion at the n^+-n junction are responsible for the ultrahigh responsivity at the

$SnSe_2/MoS_2$ heterojunction PD. The former facilitates the extraction of the photocarriers, and the latter reduces

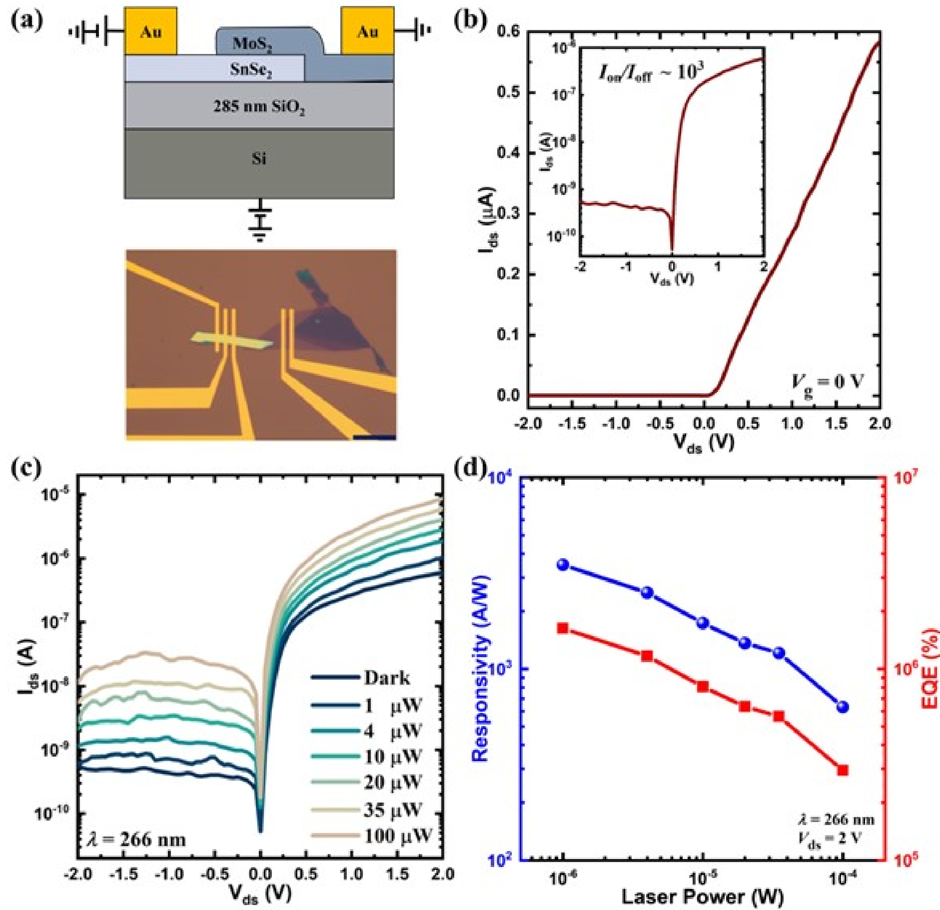

Figure 2. (a) Schematic and microphotograph of $SnSe_2/MoS_2$ heterojunction PD. The scale bar is 20 μm. (b) I_{ds}-V_{ds} curve of the $SnSe_2/MoS_2$ heterojunction diode. Inset: the semilogarithmic plot of the I_{ds}-V_{ds} curve. (c) I_{ds}-V_{ds} curves of the $SnSe_2/MoS_2$ heterojunction PD with and without laser illumination of different powers at λ= 266 nm. (d) Power-dependent responsivity and external quantum efficiency (EQE) of the $SnSe_2/MoS_2$ heterojunction PD at V_{ds} = 2V.

the tunnelling-assisted interface recombination[14]. According to the Anderson model, a unilateral depletion region is exclusively formed at the n-n or p-p junction, which reduces tunneling-assisted interface recombination and improve the responsivity of the photodetector[14,40]. Under illumination, the photogenerated electrons and holes moved to $SnSe_2$ and MoS_2, respectively, leading to an increase in the net current of the device with the increase of the illumination power

(i.e., PPC). In particular, the heterojunction device exhibits an EQE surpassing 100%, indicating the presence of a strong gain mechanism that ultimately contributes to its high responsivity. Moreover, the detectivity of the $SnSe_2/MoS_2$ PD exceeds that of $SnSe_2$ alone by three orders of magnitude because of the reduced dark current of $SnSe_2$ at the heterojunction.

In both operation modes, i.e., with and without the source-drain bias V_{ds}, the responsivity of our heterojunction PD under deep UV illumination are the highest among the reported PDs based on 2D materials and conventional semiconductors[25,41–44] (Table S1, SI). It is also comparable to the recently reported $FePSe_3/MoS_2$ heterostructure PD at the same illumination wavelength (3.36×10^4 AW^{-1} at 265 nm at $V_{ds} = 4V$)[25], in which a gold back reflector was employed to enhance the light absorption at the heterostructure and shorten the transport distance of the photogenerated charge carriers. The performance of our $SnSe_2/MoS_2$ PD could be further boosted by using a similar device configuration with a backside reflector, as it was shown in one of our recent works that such an optical cavity can greatly enhance the light matter interaction in WS_2 resulting a strong trion emission[45]. The results indicate the importance of utilizing unilateral depletion of the heterojunctions with large CBM offset to achieve high responsivity PDs. The $SnSe_2/MoS_2$ heterojunction PD has a good photoresponse under zero bias with rise and fall times of 32 and 38 ms, respectively (Figure S4a, SI), due to the high built-in potential at the n^+-n junction. A maximum responsivity of 140 mAW^{-1} is attained at V_{ds} = 0 V which is higher than most of the reported UV PDs[25,41–44].

2.3 VIS photoresponse

The photoresponse of the $SnSe_2/MoS_2$ heterojunction PD is also investigated in the visible range from λ= 450 to λ= 700 nm. The I_{ds}-V_{ds} curves at λ= 650 nm for the heterojunction PD under various illumination powers are shown in Figure 3a. The PD exhibited a significant photoresponse at different illumination powers under zero bias (V_{ds}= 0V), as shown in Figure 3b, with on/off ratio of 1.24×10^3 at 265 μW due to the high built-in potential at the junction. Figure 3c shows the increase of the short circuit current I_{sc} and open circuit voltage V_{oc} with increasing the illumination power. Despite the large CBM offset at the heterojunction (Figure 1a), the V_{oc} is relatively small, in the range of meV for all measured wavelengths. This small V_{oc} could be due to band-to-band recombination which is unavoidable and the relatively small VBM offset at the heterojunction compared to the CBM offset[46,47]. The V_{oc} can be enhanced by eliminating the Schottky barriers at TMDs/metal interfaces[48]. The photoresponse and responsivity of the heterojunction PD at other illumination wavelengths can be found in Figures S4-S6, SI. The power dependent spectral responsivities of the heterojunction PD under the self-powered operation mode (V_{ds}= 0V) for all measured wavelengths are presented in Figure 3d.

As seen in Figure 3d, the heterojunction PD shows a good photoresponse in self-powered operation mode across a wide range of wavelengths in λ= 266-800 nm. However, as the illumination wavelength approaches the band edge of MoS_2 (λ= 700-800 nm), the responsivity decreases dramatically, and for illuminations with a wavelength greater than 800 nm, the photovoltaic response disappears. This behavior is consistent with the wavelength dependent PPC/NPC transformation, which is determined by the bandgap of MoS_2 (to be discussed later).

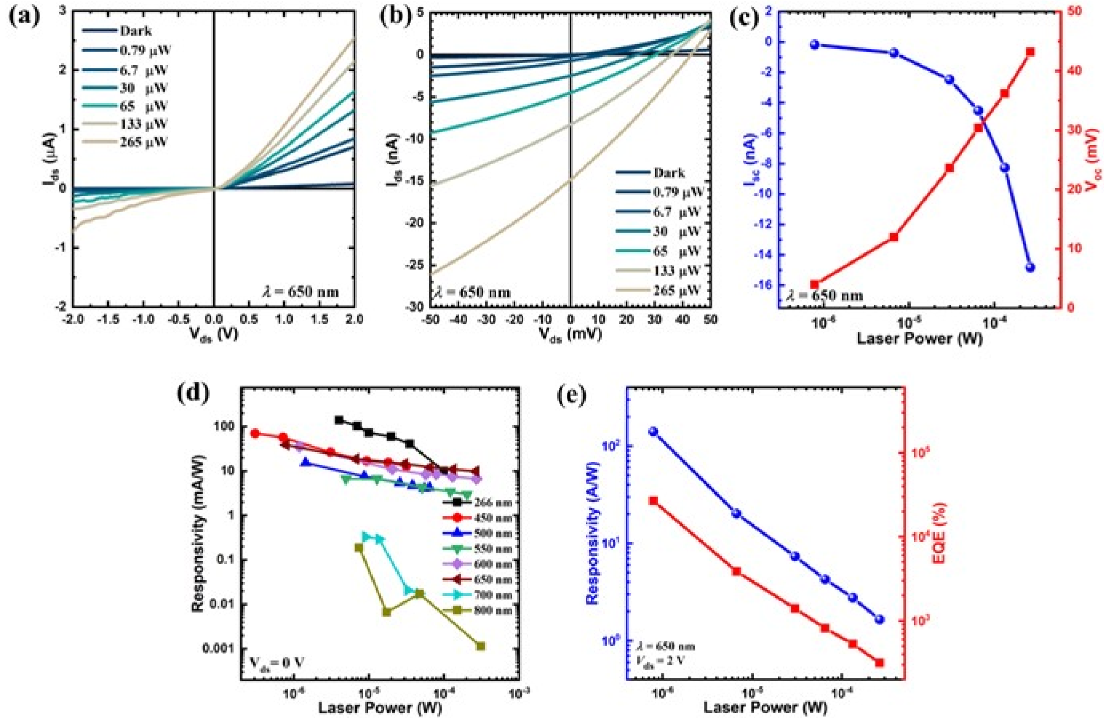

Figure 3. (a) I_{ds}-V_{ds} curves of the $SnSe_2/MoS_2$ heterojunction PD with and without laser illumination of different powers at λ= 650 nm. (b) Enlarged I_{ds}-V_{ds} curves show the self-powered response of $SnSe_2/MoS_2$ heterojunction PD at different illumination powers at λ= 650 nm. (c) The extracted short circuit current (I_{sc}) and open circuit voltage (V_{oc}) of the heterojunction PD show an increase in the I_{sc} and V_{oc} with increasing illumination power at λ= 650 nm. (d) Spectral responsivity versus illumination power of the heterojunction PD under zero bias at λ= 266-800 nm. (e) Power-dependent responsivity and EQE of the $SnSe_2/MoS_2$ heterojunction PD at λ= 650 nm and V_{ds} = 2V.

In the UV-VIS range, the responsivity of our heterojunction PD is higher than most reported self-powered PDs based on p-n or Schottky junctions[49], while the response speed is in millisecond range for all wavelengths (Figure S4a, SI) that is common for most of the reported TMD heterostructures PDs and slower than that of unilateral depletion-based heterojunction PDs[14,50]. By using bottom and top graphene electrodes in a vertical structure to reduce the transport distance of photocarriers (Figure S4b, SI), the response speed of our heterojunction PD could be enhanced.

In addition to self-powered operation, the heterojunction PD exhibits high responsivity and detectivity under applied bias of V_{ds} = 2V compared to the parent materials for all measured wavelengths (Figure S7, SI). Figure 3e shows the responsivity and EQE of the heterojunction PD

at λ= 650 nm (V_{ds} = 2V) as a function of illumination power. A maximum responsivity of 140.3 AW^{-1} and EQE of 2.7×10^4 % are achieved at illumination power of 0.79 μW with a corresponding detectivity of 8.9×10^{11} Jones. This responsivity is two orders of magnitude higher than both MoS_2 and $SnSe_2$ based PDs, which can be attributed to the effective carrier extractions at the type-II junction with large CBM offset. Likewise, the detectivity is two orders of magnitude higher than that of $SnSe_2$ based PD because of the reduced dark current at the junction. Figures S8-S12, SI, show the photocurrent and power-dependent responsivity and EQE as well as the detectivity of MoS_2 and $SnSe_2$-based PDs for all measured wavelengths.

2.4. IR photoresponse and photocurrent polarity switching

Next, we investigated the IR photoresponse of the heterojunction PD in the wavelength range from λ= 800 to λ= 1100 nm (the limit of our measurement setup). Figure 4a shows the power-dependent I_{ds}-V_{ds} curves at λ= 1100 nm. Interestingly, a transformation from PPC in the visible range to NPC in the IR was observed. With increasing the illumination power, the current gradually decreased. At a much higher illumination power of 199 μW, the current slightly increased (red dots line in Figure 4a). The inset of Figure 4a is the calculated negative photocurrent as a function of laser power. To further explore the mechanism of the NPC in our heterojunction PD, we fabricated the same device structure using slightly p doped MoS_2 (the microphotograph of the device is shown in Figure S1, SI). Figure 4b shows the photoresponse of the n^+-$SnSe_2$/p-doped MoS_2 heterojunction PD at the same illumination wavelength of λ= 1100 nm, where a similar behavior was observed without significant differences. A comparison of the responsivity and EQE of the heterojunction PDs are shown in Figure 4c. Similarly, the detectivities of the heterojunction PDs were greatly enhanced by two orders of magnitude than $SnSe_2$ PD in the IR range (Figures S7 and S12, SI) due to the significant reduction of the dark current.

To delve deeper into the dominant noise in our PDs, we conducted noise spectrum measurements for both individual materials and the heterostructure. From the noise spectra, the detectivity can be calculated using the following equation [51] :

$$D^* = \frac{R\sqrt{B\,A_{device}}}{\sqrt{\langle i_n \rangle^2}} \tag{7}$$

where, $\langle i_n \rangle^2$ and B represent the mean square noise current and the test bandwidth (15 KHz), respectively. The current spectral density (I_{SD}) of individual materials and the heterostructure is shown in Figure S13a, SI. Apparently, the noise is reduced for the heterostructure photodetector compared to the individual materials. The root mean square noise currents were calculated to be 3.33×10^{-11} $AHz^{-1/2}$, 7.87×10^{-10} $AHz^{-1/2}$, and 2.35×10^{-11} $AHz^{-1/2}$ for MoS_2, $SnSe_2$, and the heterostructure, respectively. A comparison of the calculated detectivities for the parent materials and the heterostructure as a function of wavelength is shown in Figure S13b. The detectivity values are comparable to those calculated according to equation 6, indicating that shot noise is dominant in our PDs.

The change from PPC to NPC is determined by the bandgap of MoS_2 which is consistent with the self-powered operation mode that is enabled only in the UV-VIS range. In previous reports, the mechanisms for the ambipolar photoresponse with PPC and NPC in 2D materials were attributed to the effects of adsorption[52,53] and bolometric[54]. The adsorption or desorption of moisture can alter the conductivity of semiconductors and induce NPC. However, these mechanisms can be ruled out in our heterojunction PD. As shown in Figure S14a, b, SI, for 1L MoS_2, there is no photoresponse observed in the IR range (λ > 800 nm) and a very small positive photoresponse at λ= 800 nm (the band edge of MoS_2). On the other hand, the $SnSe_2$ PD (Figure S14c, SI) did not show any NPC for all illumination wavelengths, indicating that the ambipolar

photoresponse with PPC and NPC solely exists in the heterojunction PD, and there is no contribution from the adsorption/desorption of moisture. The bolometric effect should have least effect as the SiO_2/Si substrate used has a higher thermal conductivity than flexible substrates[54].

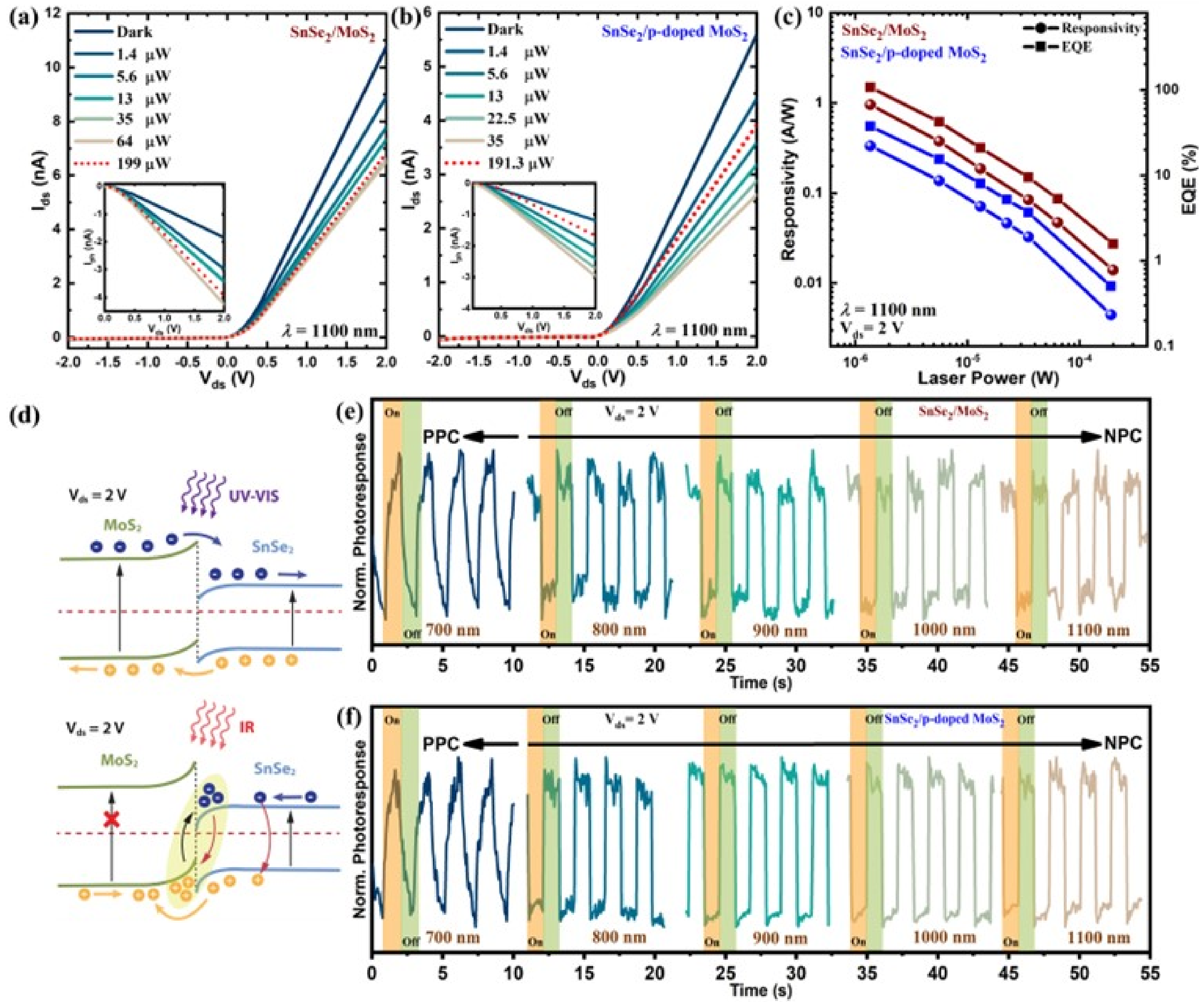

Figure 4. (a, b) I_{ds}-V_{ds} curves of $SnSe_2/MoS_2$ (a), and $SnSe_2$/p-doped MoS_2 (b) heterojunction PDs with and without illumination of different powers at λ= 1100 nm. Insets are the calculated negative photocurrent. (c) Comparison of the power-dependent responsivity and EQE of $SnSe_2/MoS_2$ and $SnSe_2$/p-doped MoS_2 heterojunction PDs at λ= 1100 nm. (d) Energy band diagrams of the $SnSe_2/MoS_2$ PD under laser illumination in the UV-VIS (top panel) and IR (bottom panel) ranges at V_{ds}= 2 V. (e, f) The photoresponse of $SnSe_2/MoS_2$ (e) and $SnSe_2$/p doped MoS_2 (f) heterojunction PDs at 1 Hz laser modulation (V_{ds}= 2 V and V_g = 0 V), showing a change in the polarity of the photocurrent from PPC in the visible range at λ= 700 nm to NPC in the IR range at λ= 800-1100 nm.

The mechanism of the observed NPC is illustrated in Figure 4d. The band alignment between the two materials before and after contact are shown in Figures S15 a and b, SI, where the Fermi levels of $SnSe_2$ and MoS_2 are located at 87 meV [28] and 0.4 eV [55] below the CBM, respectively. Besides, the band diagrams in the lateral transport direction at different bias voltages, are depicted in Figure S15c, SI. Under illumination with photon energy higher than the bandgap of MoS_2 and $SnSe_2$ (i.e., in the UV-VIS range), both materials are effectively excited, and the photogenerated electrons move to $SnSe_2$ while holes move to MoS_2, increasing the net current of the device and leading to PPC (top panel of Figure 4d). In contrast, under illumination with lower photon energy below the bandgap of MoS_2 but above the bandgap of $SnSe_2$ (i.e., in the NIR range), only $SnSe_2$ are effectively excited, and the electron-hole pairs generated from the band-to-band transition in $SnSe_2$ and the interlayer transition from the VBM of MoS_2 to the CBM of $SnSe_2$ (black arrows) are followed by a quick separation with holes flowing from $SnSe_2$ to MoS_2. The trapped charges due to the interlayer transition causes a band bending at the interface of the heterojunction (bottom panel of Figure 4d). The high density of electrons in $SnSe_2$ and holes in MoS_2 induces a recombination process (red arrows), which results in a decrease in the net current of the device and in turn the NPC (bottom panel of Figure 4d). In addition, interlayer exciton trapping at the interface could be another mechanism contributing to the NPC phenomenon, which has been observed before in WS_2/HfS_2 heterostructure under positive source-drain bias [56] and in ReS_2/$ReSe_2$ heterostructure[23].

To investigate the conversion between PPC and NPC in our $SnSe_2$/MoS_2 heterojunction PD in more detail, we conducted experiments to study the polarity switching in relation to laser wavelength, laser power and gate voltage. Figures 4e and f demonstrate the wavelength-dependent change from PPC to NPC under 1 Hz modulated laser beam at V_{ds}= 2V and V_g= 0V for $SnSe_2$/n-

MoS_2 and $SnSe_2$/p-MoS_2, respectively. The polarity of the photocurrent in both heterojunction PDs changes from PPC in the visible range at λ= 700 nm to NPC in the IR range at λ= 800-1100 nm. Notably, the response speed in the PPC operation mode is slower than that in the NPC operation mode, which can be attributed to the difference in the dynamics of charge carriers involved in each phenomenon. In the case of PPC, both materials become effectively excited, and the photogenerated carriers diffuse through the materials to reach the contacts (as depicted in the top panel of Figure 4d). The transportation of these photogenerated carriers requires time, resulting in a gradual increment in photoconductivity and, consequently, a slower response speed. Conversely, in the NPC operation mode, the reduction in photoconductivity (the number of free charge carriers available for conduction) occurs due to the charge trapping at the interface, inducing recombination (as depicted in the bottom panel of Figure 4d). The decrease in photoconductivity, particularly due to recombination, can occur on shorter timescales, leading to a faster response speed Typically, the carrier transport process occurs over a longer time compared to the recombination process [57,58], which results in a faster response speed in the NPC mode compared to the PPC mode. At a fixed wavelength of λ= 700 nm, the transition could be modulated *via* both gate voltage and laser power, as shown in Figure S16, SI. At V_g= 0 V, the PD exhibited a PPC at all illumination powers. However, under a gate voltage of V_g= -5 V, the PD showed a NPC at low illumination power (1 μW), and it switched to a PPC as the illumination power increased from 5 μW to 47 μW. When the gate voltage was further increased to V_g= -10 V, the illumination power-dependent polarity switching shifted to 9 μW. At a fixed laser power of 1 μW, the PD exhibits a PPC at $V_g \geq 0$V and a NPC at $V_g < 0$V. This observation provides strong support for the hypothesis that charge recombination and interlayer charge trapping contribute to the NPC phenomenon in our heterojunction PD. These unprecedented controllability of the switching between PPC and

NPC via multiple parameters of wavelength, gate voltage, and laser power has never been reported before in other material systems and could provide more flexibilities and functionalities for optoelectronic devices.

3. Discussion

The spectral responsivity of our PD (at $V_{ds} = 2$ V and $V_g = 0$ V) and other reported PDs is summarized in Figure 5 and Table S1, SI. Our PD has high responsivities comparable to the best-reported PDs in the entire wavelength range. In deep UV, the PD exhibits the highest value among all the reported PDs without cavity enhancement. The shaded areas in Figure 5 mark out the PPC and NPC regions in our heterojunction PD at different illumination ranges. By utilizing the unique property of PPC only in the UV-VIS range and NPC only in the IR range, a novel PD can be designed to operate differently in different wavelength bands, functioning as a day/night detector. Moreover, the PD can operate in both photovoltaic and photoconductive modes with high sensitivity. Under the self-powered operation mode, which is enabled only in the UV-VIS range, the PD can completely block any contribution from IR during the day operation mode. The comparison of the reported NPC in 2D-material based PDs is shown in Table S2, SI. Among the few reports with ambipolar photoresponse, the unique control of the ambipolar output signal in our $SnSe_2/MoS_2$ heterojunction PD through manipulating the inputs (illumination wavelength, irradiation power, and gate voltage) presents a compelling way for advancing photonic devices to enable more intricate logic computing and multi-level programming[59].

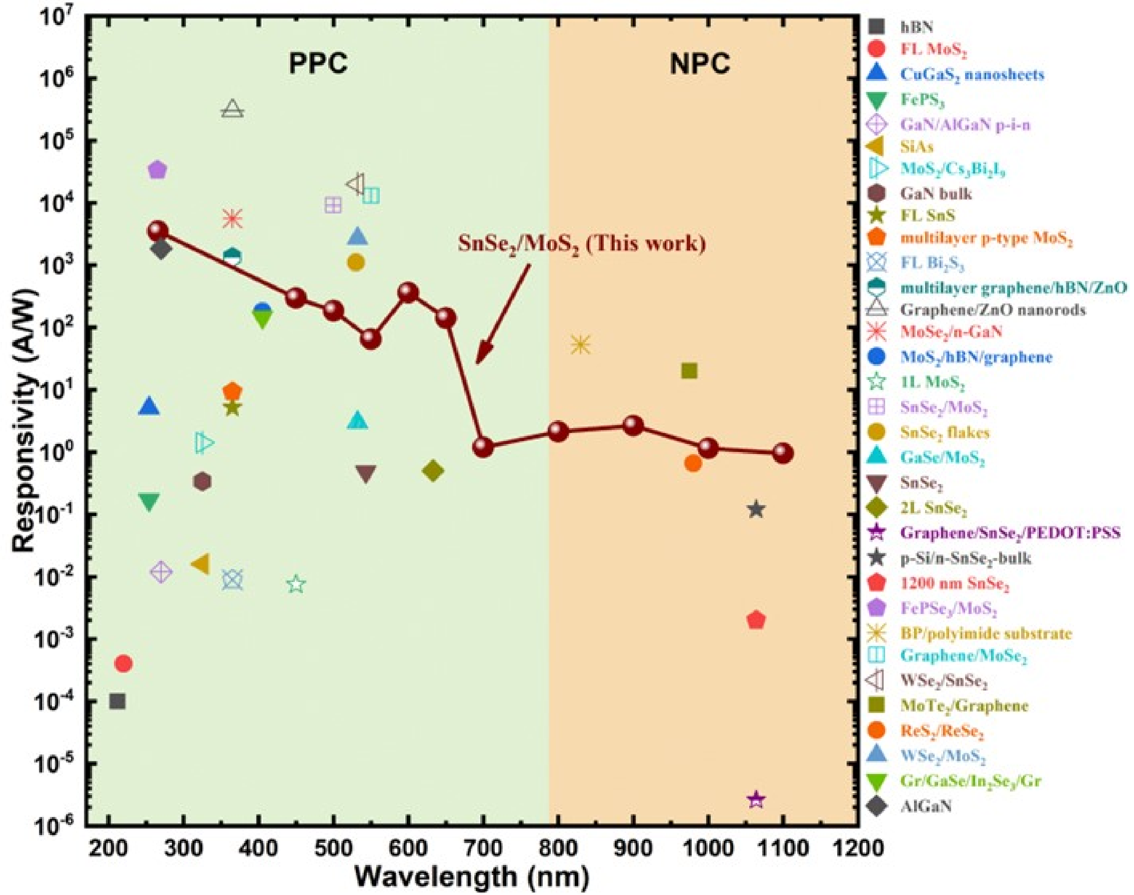

Figure 5. The spectral responsivity of our $SnSe_2/MoS_2$ heterojunction PD (V_{ds} = 2V and V_g = 0V) compared to other reported PDs. The shaded parts mark out the PPC and NPC regions at different illumination ranges (UV-VIS and IR).

4. Conclusion

We have demonstrated a high-performance PD based on a $SnSe_2/MoS_2$ van der Waals heterostructure that operates effectively across a broad wavelength range of **λ**= 266-1100 nm. The unique band alignment with large CBM offset and unilateral depletion region of the heterojunction enabled the PD to achieve a high responsivity of 3.5×10^3 AW^{-1} at **λ**= 266 nm. Besides, it operates effectively in the self-powered operation mode in the UV-VIS range due to the high built-in potential at the heterojunction. The PD exhibited a wavelength-dependent ambipolar photoresponse, with PPC in the UV-VIS range (**λ**= 266-700 nm) and NPC in the NIR range (**λ**=

800-1100 nm). Moreover, the PPC and NPC can be controlled *via* wavelength, gate voltage, and laser power. The coexistence and controllable positive and negative photoconductivity make the $SnSe_2/MoS_2$ PD a promising candidate for multifunctional optoelectronic devices.

5. Experimental Section

Device fabrication and electrical characterization: The $SnSe_2$, MoS_2, and p doped MoS_2 were exfoliated from bulk crystals (purchased from HQ graphene and 2D Semiconductors) using polydimethylsiloxane (PDMS). The dry transfer was employed to assemble the heterostructures on a pre-patterned SiO_2/Si substrate. The standard photolithography process was first used to fabricate the alignment marks and pads, which was followed by evaporation of Cr/Au (10/30 nm in thickness) and lift-off. The assembled heterostructures were annealed in a quartz chamber at 150°c under flowing Ar (200 sccm) to improve the interlayer coupling. Standard electron beam lithography was used for electrode patterning, followed by Au deposition (50 nm thick) and lift-off. The electrical properties of the fabricated devices were investigated using a Janis probe station under vacuum (~10^{-2}-10^{-3} mbar). Then the devices were fixed on chip carriers and wire bonded for photoresponse measurements. The noise spectrum measurements were conducted in dark at ambient conditions using Keithley 4200-SCS semiconductor characterization system.

Thickness measurements and optical characterization: Atomic force microscopy (AFM, Bruker Dimension ICON) was used to determine the thickness of the exfoliated flakes. Raman scattering spectroscopy and photoluminescence (PL) spectra of the samples were performed with 50x objective using Alpha 300S (WITec Gmbh) under a laser excitation at the wavelength of 532 nm.

Photoresponse measurements: To measure the broadband photoresponse ranging from λ = 450 to 1100 nm, we utilized a supercontinuum laser source (SuperK EXTREME, NKT Photonics) and multi-wavelength filter (SuperK SELECT, NKT Photonics). The laser output was focused onto the overlapping area of the heterojunction (28 μm^2) through an objective to a spot size of 150 μm for the wavelength range of 450-650 nm, and 300 μm for the range of 700-1100 nm. To ensure a reliable estimation of the responsivity for the heterojunction PD, the calculation considers the entire area of the semiconductor materials (~100 μm^2), not just the overlapping area of the junction. For deep-UV photoresponse, a laser source at the wavelength of 266 nm (FL-266-nano-50 mW) with a spot size of 1 mm diameter was used without focusing. Keithley 2450 source meters and an optical shutter were used to collect the current and modulate the laser beam, respectively.

Supplementary Information

Supporting Information is available from the Wiley Online Library or from the author.

Acknowledgements

The work is financially supported by the National Research Foundation, Singapore under its CRP program (NRF-CRP26-2021-0004), A*STAR under AME IRG Program (A20E5c0084 and A2083c0058) and GAP Funding (I21D1AG010). Y. L. acknowledges funding of A*STAR Career Development Fund - Seed Projects (C222812008). A.E. thank Prof. Cesare Soci for the valuable discussion.

Conflict of Interest

The authors declare no conflict of interest.

Author Contribution

A.E. and J.T. conceived and initiated the work; Z.W. contributed to the idea of deep-UV PD. A.E. conducted the device fabrication with the help from Y.L., H.L., Q.W, J.D., and M.J; A.E. and Z.W. setup the optical system and did the characterization with the help from X.L. and Z.O.; A.E. analyzed the data and wrote the manuscript; H.S., J.P., S.Z., and J.T. advised and supervised the work. A.E. and Z.W. contributed equally to this work. All the authors have discussed the results and revised the manuscript.

Data Availability Statement

The data that support the findings of this study are available in the Supporting Information of this article.

References

[1] F. Zhuge, Z. Zheng, P. Luo, L. Lv, Y. Huang, H. Li, T. Zhai, *Adv. Mater. Technol.* **2017**, *2*, 1700005.

[2] X. Liu, T. Galfsky, Z. Sun, F. Xia, E. Lin, Y.-H. Lee, S. Kéna-Cohen, V. M. Menon, *Nat. Photonics* **2015**, *9*, 30.

[3] Q. Qiu, Z. Huang, *Adv. Mater.* **2021**, *33*, 2008126.

[4] M. Bernardi, M. Palummo, J. C. Grossman, *Nano Lett.* **2013**, *13*, 3664.

[5] A. Chaves, J. G. Azadani, H. Alsalman, D. R. da Costa, R. Frisenda, A. J. Chaves, S. H. Song, Y. D. Kim, D. He, J. Zhou, A. Castellanos-Gomez, F. M. Peeters, Z. Liu, C. L. Hinkle, S.-H. Oh, P. D. Ye, S. J. Koester, Y. H. Lee, P. Avouris, X. Wang, T. Low, *NPJ 2D Mater. Appl.* **2020**, *4*, 29.

[6] R. Liu, F. Wang, L. Liu, X. He, J. Chen, Y. Li, T. Zhai, *Small Struct.* **2020**, *2000136*, 2000136.

[7] Y. Liu, A. Elbanna, W. Gao, J. Pan, Z. Shen, J. Teng, *Adv. Mater.* **2022**, *34*, 2107138.

[8] A. K. Geim, I. V. Grigorieva, *Nature* **2013**, *499*, 419.

[9] B. Li, L. Huang, M. Zhong, Y. Li, Y. Wang, J. Li, Z. Wei, *Adv. Electron Mater.* **2016**, *2*, 1600298.

[10] R. Cheng, D. Li, H. Zhou, C. Wang, A. Yin, S. Jiang, Y. Liu, Y. Chen, Y. Huang, X. Duan, *Nano Lett.* **2014**, *14*, 5590.

[11] C.-H. Lee, G.-H. Lee, A. M. van der Zande, W. Chen, Y. Li, M. Han, X. Cui, G. Arefe, C. Nuckolls, T. F. Heinz, J. Guo, J. Hone, P. Kim, *Nat. Nanotechnol.* **2014**, *9*, 676.

[12] A. Pezeshki, S. H. H. Shokouh, T. Nazari, K. Oh, S. Im, *Adv.Mater.* **2016**, *28*, 3216.

[13] A. Varghese, D. Saha, K. Thakar, V. Jindal, S. Ghosh, N. V. Medhekar, S. Ghosh, S. Lodha, *Nano Lett.* **2020**, *20*, 1707.

[14] F. Wu, Q. Li, P. Wang, H. Xia, Z. Wang, Y. Wang, M. Luo, L. Chen, F. Chen, J. Miao, X. Chen, W. Lu, C. Shan, A. Pan, X. Wu, W. Ren, D. Jariwala, W. Hu, *Nat. Commun.* **2019**, *10*, 4663.

[15] G. H. Shin, C. Park, K. J. Lee, H. J. Jin, S.-Y. Choi, *Nano Lett.* **2020**, *20*, 5741.

[16] Y. Yang, X. Peng, H.-S. Kim, T. Kim, S. Jeon, H. K. Kang, W. Choi, J. Song, Y.-J. Doh, D. Yu, *Nano Lett.* **2015**, *15*, 5875.

[17] G. Kim, I. G. Kim, J. H. Baek, O. K. Kwon, *Appl. Phys. Lett.* **2003**, *83*, 1249.

[18] N. K. Tailor, C. A. Aranda, M. Saliba, S. Satapathi, *ACS Mater. Lett* .**2022**, 2298.

[19] S. Ghosh, A. Varghese, H. Jawa, Y. Yin, N. V. Medhekar, S. Lodha, *ACS Nano* **2022**, *16*, 4578.

[20] Y. Wang, E. Liu, A. Gao, T. Cao, M. Long, C. Pan, L. Zhang, J. Zeng, C. Wang, W. Hu, S.-J. Liang, F. Miao, *ACS Nano* **2018**, *12*, 9513.

[21] K. Roy, M. Padmanabhan, S. Goswami, T. P. Sai, G. Ramalingam, S. Raghavan, A. Ghosh, *Nat. Nanotechnol.* **2013**, *8*, 826.

[22] H. J. Kim, K. J. Lee, J. Park, G. H. Shin, H. Park, K. Yu, S.-Y. Choi, *ACS Appl. Mater. Interfaces* **2020**, *12*, 38563.

[23] K. Li, C. Du, H. Gao, T. Yin, L. Zheng, J. Leng, W. Wang, *ACS Appl Mater Interfaces* **2022**, *14*, 33589.

[24] H. Jawa, A. Varghese, S. Ghosh, S. Sahoo, Y. Yin, N. V. Medhekar, S. Lodha, *Adv. Funct. Mater.* **2022**, *32*, 2112696.

[25] M. Long, Z. Shen, R. Wang, Q. Dong, Z. Liu, X. Hu, J. Hou, Y. Lu, F. Wang, D. Zhao, F. Ding, Y. Tu, T. Han, F. Li, Z. Zhang, X. Hou, S. Wang, L. Shan, *Adv. Funct. Mater.* **2022**, *32*, 2204230.

[26] F. A. Rasmussen, K. S. Thygesen, *The Journal of Physical Chemistry C* **2015**, *119*, 13169.

[27] J. M. Gonzalez, I. I. Oleynik, *Phys. Rev. B* **2016**, *94*, 125443.

[28] C. Guo, Z. Tian, Y. Xiao, Q. Mi, J. Xue, *Appl. Phys. Lett.* **2016**, *109*, 203104.

[29] Y. Yu, C. Li, Y. Liu, L. Su, Y. Zhang, L. Cao, *Sci. Rep.* **2013**, *3*, 1866.

[30] M. Dandu, R. Biswas, S. Das, S. Kallatt, S. Chatterjee, M. Mahajan, V. Raghunathan, K. Majumdar, *ACS Nano* **2019**, *13*, 4795.

[31] H. Li, Q. Zhang, C. C. R. Yap, B. K. Tay, T. H. T. Edwin, A. Olivier, D. Baillargeat, *Adv. Funct. Mater.* **2012**, *22*, 1385.

[32] F. Li, T.-D. Huang, Y.-W. Lan, T.-H. Lu, T. Shen, K. B. Simbulan, J. Qi, *Nanoscale* **2019**, *11*, 13725.

[33] Y. Su, M. A. Ebrish, E. J. Olson, S. J. Koester, *Appl. Phys. Lett.* **2013**, *103*, 263104.

[34] T. Pei, L. Bao, G. Wang, R. Ma, H. Yang, J. Li, C. Gu, S. Pantelides, S. Du, H. Gao, *Appl. Phys. Lett.* **2016**, *108*, 053506.

[35] C. Xie, C. Mak, X. Tao, F. Yan, *Adv. Funct. Mater.* **2017**, *27*, 1603886.

[36] M. Amani, C. Tan, G. Zhang, C. Zhao, J. Bullock, X. Song, H. Kim, V. R. Shrestha, Y. Gao, K. B. Crozier, M. Scott, A. Javey, *ACS Nano* **2018**, *12*, 7253.

[37] N. Sefidmooye Azar, J. Bullock, V. R. Shrestha, S. Balendhran, W. Yan, H. Kim, A. Javey, K. B. Crozier, *ACS Nano* **2021**, *15*, 6573.

[38] Y. Yu, T. Shen, H. Long, M. Zhong, K. Xin, Z. Zhou, X. Wang, Y. Liu, H. Wakabayashi, L. Liu, J. Yang, Z. Wei, H. Deng, *Adv. Mater.* **2022**, *34*, 2206486.

[39] K. K. H. Smithe, C. D. English, S. V. Suryavanshi, E. Pop, *2d Mater.* **2016**, *4*, 011009.

[40] B. L. SHARMA, R. K. PUROHIT, Vol. 5 (Elsevier, 2015).

[41] A. Kumar, M. A. Khan, M. Kumar, *J. Phys. D. Appl. Phys.* **2022**, *55*, 133002.

[42] H. K. Sandhu, J. W. John, A. Jakhar, A. Sharma, A. Jain, S. Das, *Adv. Mater. Interfaces* **2022**, *9*, 2102200.

[43] S. Xie, M. Shiffa, M. Shiffa, Z. R. Kudrynskyi, O. Makarovskiy, Z. D. Kovalyuk, W. Zhu, K. Wang, A. Patanè, *NPJ 2D Mater. Appl.* **2022**, *6*, 61.

[44] Y. Gao, J. Yang, X. Ji, R. He, J. Yan, J. Wang, T. Wei, *ACS Appl. Mater. Interfaces* **2022**, *14*, 21232.

[45] Z. Wang, M. Sebek, X. Liang, A. Elbanna, A. Nemati, N. Zhang, C. H. K. Goh, M. Jiang, J. Pan, Z. Shen, X. Su, N. T. K. Thanh, H. Sun, J. Teng, *Advanced Materials* **2023**, 2302248.

[46] W. Shockley, H. J. Queisser, *J. Appl. Phys.* **1961**, *32*, 510.

[47] J. Wang, *EcoMat.* **2022**, *4:e12263*, 1.

[48] S. A. Svatek, C. Bueno-Blanco, D.-Y. Lin, J. Kerfoot, C. Macías, M. H. Zehender, I. Tobías, P. García-Linares, T. Taniguchi, K. Watanabe, P. Beton, E. Antolín, *Nano Energy* **2021**, *79*, 105427.

[49] H. Qiao, Z. Huang, X. Ren, S. Liu, Y. Zhang, X. Qi, H. Zhang, *Adv. Opt. Mater.* **2020**, *8*, 1900765.

[50] M. Dai, H. Chen, F. Wang, M. Long, H. Shang, Y. Hu, W. Li, C. Ge, J. Zhang, T. Zhai, Y. Fu, P. Hu, *ACS Nano* **2020**, *14*, 9098.

[51] M. Long, Y. Wang, P. Wang, X. Zhou, H. Xia, C. Luo, S. Huang, G. Zhang, H. Yan, Z. Fan, X. Wu, X. Chen, W. Lu, W. Hu, *ACS Nano* **2019**, *13*, 2511.

[52] C. Biswas, F. Güneş, D. D. Loc, S. C. Lim, M. S. Jeong, D. Pribat, Y. H. Lee, *Nano Lett.* **2011**, *11*, 4682.

[53] A. Grillo, E. Faella, A. Pelella, F. Giubileo, L. Ansari, F. Gity, P. K. Hurley, N. McEvoy, A. Di Bartolomeo, *Adv. Funct. Mater.* **2021**, *31*, 2105722.

[54] J. Miao, B. Song, Q. Li, L. Cai, S. Zhang, W. Hu, L. Dong, C. Wang, *ACS Nano* **2017**, *11*, 6048.

[55] S. McDonnell, R. Addou, C. Buie, R. M. Wallace, C. L. Hinkle, *ACS Nano* **2014**, *8*, 2880.

[56] S. Lukman, L. Ding, L. Xu, Y. Tao, A. C. Riis-Jensen, G. Zhang, Q. Y. S. Wu, M. Yang, S. Luo, C. Hsu, L. Yao, G. Liang, H. Lin, Y.-W. Zhang, K. S. Thygesen, Q. J. Wang, Y. Feng, J. Teng, *Nat. Nanotechnol.* **2020**, *15*, 675.

[57] Y. Wang, Z. Nie, F. Wang, *Light Sci. Appl.* **2020**, *9*, 192.

[58] Y. Jiang, S. Chen, W. Zheng, B. Zheng, A. Pan, *Light Sci. Appl.* **2021**, *10*, 72.

[59] Y. Jeon, S. Kim, J. Seo, H. Yoo, *Small Methods* **2023**, *2300391*, 1.